Nanoscale

Accepted Manuscript

This article can be cited before page numbers have been issued, to do this please use: S. Deshagani, X. Liu, B. Wu and M. Deepa, *Nanoscale*, 2019, DOI: 10.1039/C8NR08645A.

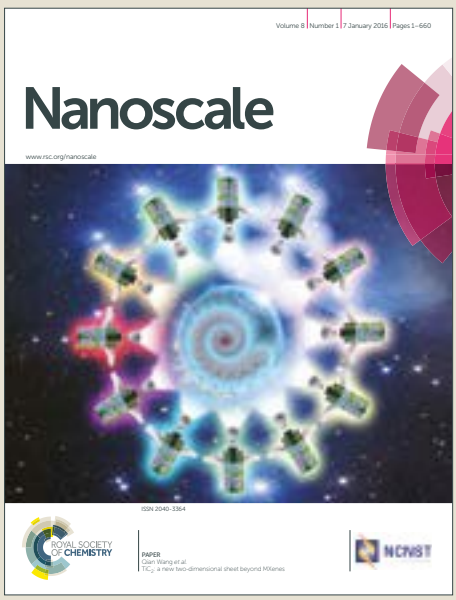

ROYAL SOCIETY OF CHEMISTRY

rsc.li/nanoscale

ROYAL SOCIETY OF CHEMISTRY View Article Online
DOI: 10.1039/C8NR08645A

Journal Name

ARTICLE

Nickel Cobaltite@Poly(3,4-ethylenedioxypyrrole) and Carbon Nanofiber Interlayer Based Flexible Supercapacitor

Sathish Deshagani,[a] Xinhua Liu,[b] Billy Wu,[b,*] Melepurath Deepa[a,*]

Received 00th January 20xx,
Accepted 00th January 20xx

DOI: 10.1039/x0xx00000x

www.rsc.org/

Abstract

Binder free flexible symmetric supercapacitors are developed with nickel cobaltite micro-flowers coated poly(3,4-ethylenedioxypyrrole) ($NiCo_2O_4$@PEDOP) hybrid electrodes. Free standing films of carbon nano-fibers (CNF), synthesized by electrospinning, were sandwiched between the $NiCo_2O_4$@PEDOP hybrid and the electrolyte coated separators on both sides of the cells. The CNF film conducts both ions and electrons, and confines the charge at the respective electrodes, to result in an improved specific capacitance (SC) and energy density compared to the analogous cell without the CNF interlayers. High SC of 1,775 F g^{-1} at a low current density of 0.96 A g^{-1} and a SC of 634 F g^{-1} achieved at a high current density of 38 A g^{-1} coupled with a SC retention of ~95% after 5,000 charge-discharge cycles in the NCO@PEDOP/CNF based symmetric supercapacitor, are performance attributes superior to that achieved with NCO and NCO/CNF based symmetric cells. The PEDOP coating serves as a highly conductive matrix for the NCO micro-flowers and also undergoes doping/de-doping during charge-discharge, thus amplifying the overall supercapacitor response, compared to the individual components. The CNF interlayers show reasonably high ion-diffusion coefficients for K^+ and OH^- propagation implying facile pathways available for movement of ions across the cross-section of the cell, and they also serve as ion reservoirs. The electrode morphologies remain unaffected by cycling, in the presence of the CNF interlayer. LED illumination and a largely unaltered charge storage response was achieved in a mutli-cell configuration, proving the potential for this approach in practical applications.

Keywords: supercapacitor; nickel cobaltite; carbon nano-fiber; energy density; conducting polymer

Introduction

Supercapacitors are ideal for emerging and existing applications such as hybrid electric vehicles, consumer electronics and even heavy-duty industrial equipment that need safe, reliable, quick bursts of power for reasonable time periods. Regarded as efficient, cost-effective and environmentally benign energy storage alternates, there is a great demand for high performance low cost materials for supercapacitors. Supercapacitors are broadly classified into two types: (i) electrochemical double layer capacitors (EDLCs) and (ii) pseudocapacitors. EDLCs offer high power densities, typically in the range of 2-10 kW kg^{-1} due to the absence of a charge transfer resistance, but suffer from low specific capacitances (SCs), and they are generally made of carbon based nano-materials[1]. To improve the SC of carbon nanostructures various modifications of the electrodes have been proposed. Hu et al., for instance, synthesized a series of multi-heteroatom porous carbon frameworks (MPCFs) from the trimerization of cyano groups of specially designed nitrogen and oxygen containing monomers followed by an ionothermal synthesis route.[2] The supercapacitor based on the MPCFs@700 electrode, delivered an energy density of 65 Wh kg^{-1} at 0.1 A g^{-1}, coupled with an extended cycling life of 10^4 cycles with 98% SC retention in an ionic liquid electrolyte. Uniform doping by nitrogen atoms in the carbon framework, imparted high electrical conductivity, and improved the SC of the electrode.[2] The same group also developed N,O-encompassing micro-porous carbon frameworks from a method involving polymerization of a monomer containing cyano groups, N- and O- atoms, followed by a high temperature treatment.[3] The porous hetero-atom containing carbon framework showed a high SC of 378 F g^{-1} in an aqueous acidic electrolyte and an enhanced cycle life of 20,000 cycles. The controlled porosity and the presence of hetero-atoms effected the excellent durability and SC performance.[3] Pseudocapacitive materials store and release charge by undergoing fast oxidation and reduction reactions at the surface of an electrode, and they offer higher energy densities compared to EDLCs but often at lower power densities due to lower electrical conductivity and charge transfer resistances. These include, transition metal oxides

[a]Department of Chemistry, Indian Institute of Technology Hyderabad, Kandi, Sangareddy-502285, Telangana (India) *Email:mdeepa@iith.ac.in

[b]Dyson School of Design Engineering, Imperial College, London. SW7 2AZ, United Kingdom *Email: billy.wu@imperial.ac.uk

like: RuO_2, MnO_2, NiO, Co_3O_4, V_2O_5, and MoO_3[4-6], as well as conducting polymers like poly(aniline) (PANI), poly(pyrrole) (PPy) and poly(3,4-ethylenedioxythiophene) (PEDOT)[7]. Designing and implementing supercapacitor architectures based on a combination of pseudocapacitive and EDL based materials enables the retention of the high energy density of the oxide or polymer without sacrificing the power density afforded by the carbon nano-material [8].

Among carbon nano-materials, activated carbon, carbon nanotubes and reduced graphene oxide are widely used in supercapacitors owing to their high cycling stability and power density despite the low energy density (3-5 Wh kg^{-1})[9,10]. Transition metal oxides such as RuO_2[11], NiO[12] and MnO_2[13] are attractive for pseudocapacitive applications due to their high theoretical SCs of 2,000, 2,935 and 1,100 F g^{-1} respectively. While RuO_2 has excellent storage characteristics[14], its high cost limits commercial applicability. Most of the metal oxides also have low electrical conductivities, which affects their performances. Binary metal oxides such as $NiCo_2O_4$, $MnCo_2O_4$, $CuCo_2O_4$, and $ZnCo_2O_4$[4] offer improved conductivities and better performances compared to the individual metal oxides. Of the binary oxides of cobalt, nickel cobaltite or $NiCo_2O_4$ (NCO) is promising due to the low cost, ease of preparation and good electrical conductivity[15]. Furthermore, it has been shown in the past that this mixed metal oxide shows better performance compared to that of the pure NiO and Co_3O_4[16]. The electrical conductivities were found to increase from 3.1×10^{-5} and 0.1 S cm^{-1} for NiO and Co_3O_4 respectively to 0.3 S cm^{-1} in $NiCo_2O_4$[17].

By considering the above-described possibilities for supercapacitors, a novel supercapacitor architecture was designed and implemented in this work. Multi-layer pseudocapacitive electrodes of NCO@poly(3,4-ethylenedioxypyrrole) or PEDOP supported over Ni foam, with an integrated free standing carbon nano-fiber (CNF) film were assembled into symmetric supercapacitors for the first time. Compared to the exhaustively explored PEDOT, its' pyrrole counterpart, PEDOP is comparatively less studied, despite a couple of advantages. PEDOP, for instance, has a lower oxidation potential than PEDOT[18] and is even more robust than PEDOT in the doped state. Furthermore, in the doped state, it is electrically conducting, and like PEDOT, it is capable of doping and de-doping anions on its π-conjugated polymer chains, and can behave as a pseudocapacitor[19]. Ultrathin, lightweight and porous CNF interlayers enhance the SC of NCO@PEDOP, by confining the redox materials (NCO and PEDOP) to the Ni foam. They serve as additional electrolyte reservoirs, and since they conduct both ions and electrons, they ensure uniform ion and electron movement across the electrode cross-sections. Compared to literature studies on pure NCO and NCO composite electrodes with conducting polymers like PPy, the symmetric cell consisting of NCO@PEDOP/CNF electrodes not only delivers an impressive specific capacitance but it also exhibits high cycling stability and flexibility. An exemplar application is shown whereby a LED is illuminated to show the viability of this scalable architecture for practical applications.

Experimental

Chemicals

Nickel (II) nitrate hexahydrate ($Ni(NO_3)_2.6H_2O$), Cobalt (II) nitrate hexahydrate ($Co(NO_3)_2.6H_2O$), EDOP (3,4-ethylenedioxypyrrole), $LiClO_4$, KOH, Agar, water, acetonitrile, Sodium dodecyl sulfate (SDS) and GF/D membranes (1.2 mm thickness) were procured from Sigma Aldrich and used directly. Ultrapure water (resistivity ~18.2 MΩ cm) was obtained through a Millipore Direct-Q3 UV system. Nickel (Ni) foam with a 1 mm thickness was purchased from Gelon.

Synthesis of $NiCo_2O_4$ (NCO) micro-flowers

NCO micro-flowers were synthesized by using a previously reported method[20]. SDS (1 mmol), $Ni(NO_3)_2.6H_2O$ (2 mmol), $Co(NO_3)_2.6H_2O$ (4 mmol), and urea (12 mmol) were dissolved in deionized water under magnetic stirring for 30 min in air. The resulting pink-red solution was transferred into a 100 mL Teflon-lined stainless-steel autoclave and a 5.0 × 5.0 cm Ni foam substrate was immersed in the solution. The autoclave was heated at 120 °C inside a hot-air oven for 15 h, and then cooled to room temperature. Subsequently, the green colored cobalt-nickel hydroxide precursor was coated over the Ni foam which was carefully extracted from the solution and washed repeatedly with deionized water. The NCO precursor coated Ni foam substrate was then annealed at 350 °C in a tube furnace for 2 h in an argon atmosphere. An electrode consisting of NCO micro-flowers coated over a Ni foam was subsequently obtained, which was again washed with deionized water, dried in a hot-air oven at 60 °C for a few hours and the electrodes were cut into desired dimensions and used. NCO films were also deposited over flat stainless steel substrates; with the product subsequently scraped off for structural characterization.

Free standing CNF films

A CNF precursor solution was prepared by mixing 0.6 g polyacrylonitrile (PAN) in 6 mL dimethylformamide (DMF) at 60 °C for 12 h. The as-prepared precursor solution was then filled into a syringe (6 ml) and driven into the needle by a syringe pump with a flow rate of 0.75 ml/h. A 13 kV potential was then applied between the metal syringe and an aluminium collector plate, separated by 17.5 cm, for 30 minutes to achieve free-standing electrospun nano-fiber mats.

To prepare conductive carbon fiber films, the nano-fiber mat was pre-carbonized in air at a ramp rate of 1 °C min^{-1} to 280 °C and held for 2 h, then post-carbonized in 0.2 L min^{-1} of N_2 at ramp rate of 2 °C min^{-1} to 550 °C, held for 1 h and the then temperature was increased to 850 °C at a ramp rate of 3 °C min^{-1} and held for 2 h.

PEDOP@NCO hybrid and fabrication of cells

EDOP (0.1 M) and $LiClO_4$ (0.1 M) were dissolved in acetonitrile (30 mL) and sonicated for 15 min. A NCO coated Ni foam electrode with an active area of 1.5 cm^2, was immersed in the solution and employed as a working electrode for an electropolymerization process. A Pt rod was used as the counter electrode and an Ag/AgCl/KCl electrode was used as the reference. Hybrid films of NCO@PEDOP were obtained under potentiostatic conditions at room temperature in a chronoamperometric mode by application of a fixed voltage of

View Article Online
DOI: 10.1039/C8NR08645A

+1.0 V to the working electrode for 500 s. The electrode was heated at 70 °C for 12 h in a vacuum oven to yield the NCO@PEDOP electrode. Similar electrodes were also obtained over NCO coated SS substrates, for characterisation. Pristine PEDOP electrodes were obtained by using the same procedure described above but with a blank Ni foam or SS plate as the working electrode. A K^+ conducting gel electrolyte was prepared by first dissolving 3 M KOH in deionized water at room temperature followed by the addition of 1.5 wt% of Agar. The mixture was continuously stirred for 5 h at 60 - 70 °C till the Agar dissolved, and yielded a viscous, brown colored gel. The gel was cooled to room temperature and stored at the same temperature. Symmetric supercapacitor cells were fabricated in the following configurations: NCO//NCO, NCO/CNF//CNF/NCO, NCO@PEDOP/CNF//CNF/NCO@PEDOP. Prior to assembly of the cells in these configurations, the gel was applied to the individual redox active (NCO or NCO@PEDOP) and CNF layers and the electrolyte was allowed to spread and seep through the electrodes for several mins. The K^+ gel was also applied to both sides of a GF/D separator and it was then sandwiched between the electrolyte rich active electrodes of a given cell. The assembly was allowed to rest for 3 to 4 h before use.

Instrumentation techniques

X-ray diffraction patterns of the active materials were recorded on a PANalytical, X'PertPRO instrument with Cu-Kα (λ = 1.5406 Å) radiation. Raman spectra were recorded for the active materials on a Bruker Senterra Dispersive Raman Microscope spectrometer. A laser excitation wavelength of 532 nm was used. Surface morphology of the active materials was studied using scanning electron microscopy (Carl Zeiss EV018 SEM). High resolution transmission electron microscopy (HRTEM) images were obtained on a FEG-TEM 300 kV-8 microscope operating at an accelerating voltage of 300 kV by using samples deposited over carbon coated copper grids. Galvanostatic charge-discharge, cyclic voltammetry (CV), self-discharge, cell durability, leakage current, I-V measurements and electrochemical impedance spectroscopy (EIS) studies were performed on an Autolab PGSTAT 302N potentiostat-galvanostat-frequency response analyzer.

Results and discussion

Structural features of the electroactive materials

The SEM image of the hydrothermally synthesized NCO (Figure 1a) shows the mixed metal oxide to have a flower like micro-sphere morphology with long needle like petals. These 3D flower-like microstructures have diameters in the range of 2 to 4 μm. During the hydrothermal synthesis, a nucleation-dissolution-recrystallization mechanism results in the formation of these microstructures[21]. SDS, the surfactant, serves as a structure directing agent and helps in attaining an open porous network of NCO micro-flowers. PEDOP is electropolymerized over the NCO coated Ni foam. The SEM image of the NCO@PEDOP electrode (Figure 1b) shows the mesh like framework of Ni struts (in the Ni foam) coated with the polymer and metal oxide particles, in striking contrast with the pristine Ni foam substrate where the Ni struts are flat and smooth (inset of Figure 1b). No uncoated areas are visible over the Ni struts, implying that optimum loading of the redox active materials is achieved over the Ni foam, and this is expected to maximize capacitance, during electrochemical cycling.

The TEM images of NCO (Figure 1c,d) show the distinct flower like shapes, composed of needle like structures compactly packed particularly at the middle portion of the flowers. The needle like shapes appear to be supported over sheet like structures. The size of the micro-flowers vary from 2 to 4 μm, which is line with the SEM results. The magnified view of the NCO micro-flowers (Figure 1e), reveals them to be constituted by irregular shaped nanoparticles but arranged such to give an elongated appearance. The particles are 10 to 15 nm in dimensions; they are overlapping and densely packed. A lattice scale image of the NCO (Figure 1f) shows an inter-fringe distance of 0.2 nm, which aligns with the (400) plane of spinel NCO. The NCO micro-flowers are polycrystalline, and this is confirmed from the electron diffraction (SAED) pattern of the selected area presented in Figure 1g. The pattern is made up of multiple spots superimposed over concentric diffuse rings. The spots are indexed to the (220), (400), (331) and (422) planes of spinel NCO. The TEM image of pristine PEDOP (Figure 1h) shows a contiguous network of cauliflowers like shapes. The grain boundaries are indistinguishable. The TEM image of the NCO@PEDOP (Figure 1i) shows the NCO flowers to be dominant, and the polymer coating is faintly perceptible near the edges of micro-flower like shapes of NCO. A high magnification image of this hybrid shows misshaped particles and needle like shapes to be embedded over sheets, indicating a good mixing of the polymer and oxide at the nano-scale. The lattice scale image extracted from the hybrid electrode (Figure 1k) displays an inter-fringe distance of 0.2 nm coinciding with the (400) plane of NCO.

Besides the NCO based electrodes, a free standing film of CNF was also employed in the symmetrical supercapacitors. While morphological and electrochemical characterization of this film is undertaken in a later section, here some structural aspects were studied. Figure 2a shows the XRD patterns of NCO, NCO@PEDOP, CNF and PEDOP. For pristine NCO, diffraction peaks at 2θ values of 31.15°, 36.69°, 44.62°, 55.44°, 59.1° and 64.98° are indexed to the (220), (311), (400), (422), (511) and (440) crystalline planes of $NiCo_2O_4$ with a spinel phase (JCPDS 20-0781). The NCO data agrees well with TEM observations. Pristine PEDOP shows a very broad diffraction peak at 2θ of 21.48° implying that the polymer is largely amorphous. The positions and relative intensities of these peaks remain unaltered when PEDOP is coated over NCO in NCO@PEDOP. The low 2θ diffraction peak from PEDOP is obfuscated by the diffraction pattern of NCO in the hybrid. The CNF film shows a broad diffraction peak at 2θ of 25.6°, which matches with an inter-planar spacing (d) of 3.34 nm corresponding to the (002) reflection of graphite (JCPDS: 75-1621). Since the peak is very broad, we deduce that the CNF film has a mixed graphitic and disordered structure as highlighted by Liu et al[22].

Raman spectra of the PEDOP (Figure 2b) shows peaks at 869 and 1,017 cm^{-1}, which are assigned to the oxyethylene ring deformation, the C-O-C deformation mode and a peak at 1,214

cm^{-1} involves overlapping contributions from C_α-C_α' inter-ring stretching and C_β-H bending modes respectively. The C_β-C_β and C_α=C_β (−O) stretching modes produce peaks at 1,370 and 1,418 cm^{-1}. A broad peak is observed at 1,580 cm^{-1} corresponding to the C-NH deformation mode. The above assignments are close to the experimental Raman data of PEDOP films doped by ClO_4^- ions[23]. The Raman spectrum of NCO (Figure 2c) displays peaks at 185, 478, 529, and 668 cm^{-1} which are attributed to the F_{2g}, E_g, F_{2g}, and A_{1g} modes of $NiCo_2O_4$ respectively. These peaks concur reasonably well with the Raman spectral data observed for NCO Nanowires prepared by facile hydrothermal synthesis in a previous report[24].

Conductivities of the active materials and gel

The I-V characteristics of the NCO and PEDOP were recorded by compactly packing the active material in a rectangular cavity of 0.5 × 0.5 cm area (a). The walls of the spacer-cavity were created by employing electrically insulating adhesive double-sided tape stuck on a flat stainless steel (SS) substrate. The thickness (l) of the tape is 0.2 cm. After packing the material, a SS plate was fixed on top of the SS, and I-V plots were recorded (Figure 2d). For the CNF film, the film was directly sandwiched between two SS plates by carefully avoiding shorting of the two SS plates. The thickness of the CNF film is ~0.1 mm. Linear I-V trends are observed in all three materials between ±0.5 V and is indicative of ohmic behaviour. From the slopes in these regions, and by using the following relations: $1/R = \Delta I/\Delta V$ and $\sigma = 1/\rho = (1/R) \times (l/a)$, the electrical conductivities were calculated. The magnitudes of conductivities are: 8 mS cm^{-1} (CNF), 26.8 mS cm^{-1} (PEDOP) and 9 mS cm^{-1} (NCO) respectively. Since these are 3 different electroactive materials, their conduction mechanisms and conductivities vary. The CNF film is electrical conductive due to the graphitic structure of the carbon nano-fibers, and the contact points within the fiber like morphology. In the graphitic structure, the carbon atoms are sp^2 hybridized and arranged in a hexagonal lattice. Each carbon atom is bonded to 3 other carbon atoms via σ-bonds in the plane, and the fourth electron resides in the unhybridized π-orbital projected above and below the plane. These electrons are therefore free to move between the graphitic layers, thus imparting electrical conductivity to the material. Besides this factor, at the macroscopic level, the material is composed of an interconnected network of carbon fibers, which also allows facile transfer of electrons between any two or more fibers in direct contact, thus contributing to the observed conductivity. PEDOP is conductive due to the fact that it is prepared by oxidative electropolymerization, and in the as-fabricated state, it comprises of many radical cation units which are charge compensated (or doped) by counter ions or in this case, ClO_4^- ions. The electrons on the radical cation units are delocalized over the monomer units in the polymer chains, thus rendering it to be conductive. NCO is conductive possibly due to the ease with which the two cations, Ni and Co can adopt two different valence states, namely +2 and +3[25], thereby making electron movement facile between the metal ion sites in the lattice structure.

A K^+-gel was employed in this study as the electrolyte for all the supercapacitors. Representative I-V plots acquired at 25 °C for the 3 M K^+-gel and liquid electrolytes are presented in Figure 2e. This was accomplished by sandwiching the liquid or gel electrolyte in cavities (made up of adhesive tape with thickness: of 0.2 cm) of 2.25 cm^2 area between two SS plates. The plots are almost linear over the voltage window of −0.2 to +1.2 V. The sharp increase in the currents at the limiting voltages is likely due to a decomposition reaction as the electrolyte is aqueous. The ionic conductivities of the 3 M K^+-gel containing 1.5 wt% of Agar, and the analogous liquid electrolyte without Agar were measured as a function of temperature, from 10 to 60 °C. Nyquist plots were recorded at different temperatures after allowing the above-described assembly to reach the required temperature, and maintaining the same temperature for 10 min. Plots were collected over a frequency range of 1 MHz to 1 Hz, under an AC excitation amplitude of 10 mV under open circuit voltage. The point of commencement of the Z″ versus Z′ curve represents the high frequency resistance behaviour. As can be observed from Figure 2f, at any given temperature, the difference between the ionic conductivities for the liquid and gel electrolytes is not very large except at 60 °C. While the ionic conductivity of the gel electrolyte is comparable to that of the liquid, the gel has the added benefit that it can enable the fabrication of a leak proof supercapacitors, as the viscosity of the gel is far higher than the corresponding liquid electrolyte. This is apparent from a photograph of an inverted beaker containing the K^+-gel (inset of Figure 2e); the gel remains intact and does not flow downwards easily. The ionic conductivity of the gel drops from 0.073 to 0.043 mS cm^{-1}, and for the liquid, it declines from 0.087 to 0.048 mS cm^{-1}, when the temperature is changed from 60 to 10 °C. The room temperature ionic conductivities are almost equal (~0.063 S cm^{-1}) for the gel and the liquid electrolytes. The conductivity of the liquid electrolyte is lowered due to the ease of ion-pairing, with the neutral ion-pairs not contributing to the ionic conductivity. The properties of the gel render it to be a suitable candidate for supercapacitors.

Supercapacitor charge-discharge behaviour

Binder free symmetric cells were constructed with NCO, NCO/CNF, and NCO@PEDOP/CNF electrodes, where the CNF interlayers were employed to enhance capacitance. The cell configurations of these 3 cells are illustrated through schematics shown in Figure 3(a-c). CV plots of the cells recorded at different scan rates of 5, 10, 50, 100 and 500 mV s^{-1} over a voltage window of 0 to 2 V are presented in Figure 3(d-f). The voltage window or ΔV is 2 V, which is higher than the usually reported span in the range of 0.5 to 1 V for NCO based supercapacitors[26,27]. The enhanced voltage window is expected to increase the energy density of the cell. All the 3 cells show rectangular leaf-like shapes at all scan rates. At low scan rates, the pristine NCO based cell shows a broad oxidation peak at a E_{ox} of +1.14 V, and in the reverse scan, E_{red} is observed at +0.91 V. This peak is also visible for the NCO/CNF cell, but somewhat obscured by PEDOP in the NCO@PEDOP/CNF cell. PEDOP shows featureless CV plots, and these are shown for a symmetric PEDOP//PEDOP cell in Figure S1 (supporting information). The redox reactions of NCO in an alkaline electrolyte are summarized below.

$$NiCo_2O_4 + OH^- + H_2O \leftrightarrows NiOOH + 2CoOOH + e^- \quad (1)$$

$$CoOOH + OH^- \leftrightarrows CoO_2 + H_2O + e^- \quad (2)$$

The charge-discharge curves for the three symmetric cells obtained at different current densities from 1.25 to 50 A g^{-1} and 0.96 to 38 A g^{-1} (for NCO/NCO and (NCO/CNF, NCO@PEDOP/CNF respectively.) are shown in Figure 3(g-i). The current densities were applied to the cells by considering the weights of active materials/layers for all cells under investigation. The masses were determined by weighing the Ni foam substrates before and after the deposition of the active material for NCO and NCO@PEDOP. CNF is a free standing film, which was weighed directly before it was incorporated into the cell. The mass of the active material was maintained at 2 mg for the cells with NCO and NCO@PEDOP deposited over Ni foam based electrodes. For the two cells with CNF, the mass was 2.6 mg. The profiles have quasi-triangular shapes in the 2 V voltage window. The profiles observed for NCO and NCO/CNF are similar, but the NCO@PEDOP/CNF cell shows altered charging and discharge curves due to the presence of the conducting polymer. The Ohmic drop in the discharge curve is 0.5 V for the NCO and NCO/CNF based cells; however it is 0.3 V for the NCO@PEDOP/CNF cell at 0.96 A g^{-1}. The specific capacitances (SC) were calculated using the expression provided below.

$$SC = I \text{ (current density, A } g^{-1}) \times \Delta t \text{ (discharge time, s) } / \Delta V \text{ (voltage window, V)} \quad (3)$$

For the NCO based cell, SC progressively increases from 225 to 1,453 F g^{-1}, with decreasing current density (50 to 1.25 A g^{-1}) over a voltage window of 2 V. The NCO/CNF, NCO@PEDOP/CNF based cells deliver SCs that vary from 461 to 1,554 F g^{-1} and 634 to 1,775 F g^{-1}, respectively, again over the 2 V window and when current density is changed from 38 to 0.96 A g^{-1}. The role of the CNF in improving the charge storage capability of the NCO//NCO cell is reflected in the 1.22 times enhancement in SC (at 0.96 A g^{-1}), achieved when the CNF interlayers are included in the cell to yield the NCO/CNF//CNF/NCO configuration. The contribution of PEDOP in further improving the SC is realized from the 1.14 times increment observed by including PEDOP in the cell as in the NCO@PEDOP/CNF//CNF/NCO@PEDOP supercapacitor. At higher current densities, the roles of CNF and PEDOP in controlling the storage behaviour of NCO are more obvious. At 38 A g^{-1}, CNF brings about a 3-fold improvement in the SC of the NCO cell, and PEDOP increases the SC by 1.78 times. PEDOP functions as a highly conducting matrix for the NCO micro-flowers, by allowing unhindered charge transport between the NCO particles, by the virtue of its' high electrical conductivity. It also, to some extent, prevents the aggregation of NCO particles, thus maximizing lifetime and utilization of the electroactive sites during charge-discharge, which results in an improved performance for the NCO@PEDOP/CNF cell relative to the NCO/CNF cell.

Cyclic voltammograms recorded at different scan rates and galvanostatic charge-discharge studies for the NCO@PEDOP based symmetric cells are shown in Figure S2 of the supporting information. The CV plots are nearly rectangular at high scan rates of 50, 100 and 500 mV s^{-1}, and at low scan rates of 5 and 10 mV s^{-1}, distinct oxidation and reduction peaks are observed, due the redox reactions of NCO. The NCO@PEDOP cell delivers a SC of 1,617 F g^{-1} at 1.25 A g^{-1}; this SC value is higher than that of sole NCO and NCO/CNF, but lower than that of NCO@PEDOP/CNF. This shows that both PEDOP and CNF improve the energy storage performance of NCO. The 11% increase in SC, ongoing from NCO to NCO@PEDOP illustrates that PEDOP contributes to SC either by undergoing redox reactions or by forming an EDL.

Comparison of performance parameters

The rate capability plots for the 4 symmetric cells are compared in Figure 4a. The SCs of the cells follow the following trend: NCO@PEDOP/CNF > NCO@PEDOP > NCO/CNF > NCO. This plot clearly shows that the CNF interlayer helps in increasing the SC of NCO and NCO@PEDOP electrodes. The porous CNF layer is a mixed conductor: it conducts both ions and electrons. It is in direct intimate contact with the NCO or NCO@PEDOP electrodes. Therefore, during electrochemical cycling, electrons from the external circuit reach the NCO or NCO@PEDOP materials, as they are in electrical contact with the Ni foam current collector. Since the CNF interlayer is electrically conducting, and it is physically in direct contact with these redox active materials in a given cell, electrons are easily transmitted to the CNF interlayer. Simultaneously, charge compensating cations or K^+-ions from the electrolyte are transported through the CNF interlayer and then to the NCO or NCO@PEDOP. The CNF interlayer is porous (which is confirmed from its' morphology shown in Figure 6a, b), and therefore electrolyte penetration is facile. It also serves as an additional electrolyte reservoir for K^+-ions which is advantageous considering the high capacitance of the NCO material which risks depleting the charge carriers in the electrolyte. Furthermore, the pores in the pristine Ni foam are also not completely blocked by the NCO or NCO@PEDOP coatings, enabling the electrolyte to have access across the thickness of the Ni foam coated with NCO or NCO@PEDOP. NCO and PEDOP are redox-active, and therefore they store and release charge by undergoing oxidation and reduction reactions and through a fast surface reaction mechanism. The SC observed, particularly for the symmetric NCO@PEDOP/CNF//CNF/NCO@PEDOP cell is higher than that reported for NCO based cells in previous reports. This comparison is tabulated in Table S1 (supporting information).

Ragone plots of energy density (E) versus power density (P) for the 4 symmetric cells based on NCO//NCO, NCO/CNF//CNF/NCO, NCO@PEDOP//NCO@PEDOP and NCO@PEDOP/CNF//CNF/NCO@PEDOP are shown in Figure 4b. E and P were estimated using the formulae given below.

$$E \text{ (Wh kg}^{-1}) = SC \times \Delta V^2 \times 1000 / 2 \times 3600 \quad (4)$$

$$P \text{ (W kg}^{-1}) = 3600 \times E / \Delta t \quad (5)$$

Power density of all the 4 symmetrical cells lies in the range of 1.25 to 50 and 0.961 to 38 kW g^{-1} when current density is increased from 1.25 to 50 A g^{-1} (for NCO/NCO, NCO@PEDOP) and 0.96 to 38 A g^{-1} (for NCO/CNF, NCO@PEDOP/CNF) respectively, over voltage windows of 2 V. Measured power density is not necessarily completely governed by the material type and crucially also depends on (i) the voltage window of cell operation and (ii) applied current density. Energy density is controlled by material type. For the NCO/CNF and

NCO@PEDOP/CNF based symmetrical supercapacitor, energy density decreases from 863 to 256 and 986 to 352 Wh kg^{-1} when the current density is increased from 0.96 to 38 A g^{-1}, over the 2 V range. Energy density varies from 807 to 124 and 898 to 125 Wh kg^{-1} over the same voltage window and when current density increased from 1.25 to 50 A g^{-1} for the NCO and NCO@PEDOP based symmetrical supercapacitors (at 1.25 to 50 kW kg^{-1} power density). Such a high energy density of 352 Wh kg^{-1}, especially achieved by the NCO@PEDOP/CNF//CNF/NCO@PEDOP cell, at a fairly high current density of 38 A g^{-1}, is a remarkable storage attribute[28-32]. The highest energy density of the symmetric NCO@PEDOP cell is 898 Wh kg^{-1} at a power density of 1.25 kW kg^{-1}; this again is lower than that of the corresponding cell with CNF.

Leakage current and self-discharge are two performance parameters that must be analyzed when evaluating the potential of a given supercapacitor for real time applications. Leakage current is the current needed to maintain a constant voltage, and it is also directly proportional to cell capacitance. Here, from the fully charged state of 1.5 V, when the leakage current is measured as a function of time (Figure 4c), the initial magnitude is almost ~0.01 A for the NCO@PEDOP/CNF cell. Leakage current for the NCO@PEDOP/CNF based cell shows a stable value of 5×10^{-5} A after 60 min. Leakage current is better stabilized for the conducting polymer based cell, implying that PEDOP has better charge retention characteristics.

Self-discharge is the voltage drop that a charged cell experiences as a function of time under zero load conditions. Self-discharge profiles of the 3 cells when they were allowed to discharge under zero external current (Figure 4d), from 1.5 V onwards, are shown in Figure 4d. The NCO@PEDOP/CNF cell discharges to ~0.5 V in 2.5 min, and the NCO/CNF and NCO cells reach this value at faster rates (in 0.35 and 0.19 min respectively). These differentials again show that both CNF and PEDOP assist in retaining the charged state of the NCO based cell. Furthermore, self-discharge rate is controlled by the leakage current and charge redistribution. The charge redistribution corresponds to the displacement of charges from an easily accessible charged region of the electrode with a low access time constant, to a more difficult one, with a longer time constant. This mode is probably active in the PEDOP based cell, which results in the desirable slow self-discharge performance. The parameters are provided in Table 1.

Impedance studies

Nyquist plots were recorded for 4 symmetric cells before and after they were cycled 5000 times. The plots were recorded under an AC amplitude of 10 mV applied over a frequency range of 1 MHz to 0.1 Hz (with a 0 V DC bias). Figure 4 e,f shows the Z″ versus Z′ curves for the cells. All the three cells show an arc in the high frequency domain, followed by an inclined straight line. The high frequency intercept on the Z′ axis is the gel electrolyte resistance (R_S) and upon extrapolating the low frequency straight line data onto the abscissa, the intercept obtained is labelled as R_i. By employing the relation: $R_\Sigma = 3 (R_i - R_s)$, R_Σ, the ionic diffusion resistance is determined. The magnitudes of R_Σ before cycling are 0.09, 0.18, 0.51 and 0.06 Ω for the NCO, NCO/CNF, NCO@PEDOP and NCO@PEDOP/CNF based cells respectively. After cycling, R_Σ increases to 1.11, 0.45, 1.36 and 0.9 Ω for the NCO, NCO/CNF and NCO@PEDOP/CNF cells respectively. R_Σ is the lowest for the NCO@PEDOP/CNF cell and highest for the NCO based cell, indicating that K^+ or OH^- ion-propagation is facile across the CNF interlayer, due to the pores present in the CNF film. These low magnitudes of R_Σ observed for the CNF based cells also indicate that interfacial resistance at the NCO or NCO@PEDOP and CNF interlayer is negligible, for had this interface offered significant resistance to ion and electron movement, then it would have reflected in the R_Σ magnitudes. After cycling, R_Σ increases for all cells, and this is because repetitive ion insertion and extraction during charge-discharge is accompanied by volume enlargement and shrinkage, and electrolyte decomposition also occurs, resulting in a loss of inter-particle contact thus adversely impacting the electrochemical performance.

Cycling stabilities of the 4 symmetric cells with NCO, NCO/CNF, NCO@PEDOP and the NCO@PEDOP/CNF are compared in Figure 5a. The SCs for the cells are plotted as a function of cycle number, over 5,000 charge-discharge cycles operated at a constant current density of 20 A g^{-1}. The NCO@PEDOP/CNF cell shows good durability, as the capacitance fade with cycling is almost insignificant for this cell, and negligible for the NCO cell. After 5,000 cycles, 98, 99.3 and 99% of their initial capacitances are retained for the NCO/CNF, NCO@PEDOP and the NCO@PEDOP/CNF cells. The sole NCO based cell retained 96% of its' original capacitance. Aggregation of the metal oxide particles at the active cites during charge-discharge and the delamination of NCO from the current collector are the reasons for the lowered cycling performance. The presence of PEDOP in the hybrid prevents aggregation of NCO and the CNF interlayer also assists in preventing NCO or NCO@PEDOP from detaching from the Ni foam fibers, thus leading to improved durability.

To understand the improved performance and durability induced by PEDOP and CNF, SEM images of the NCO@PEDOP/CNF, NCO/CNF, NCO@PEDOP, NCO and CNF interlayer, were recorded after 5,000 charge-discharge cycles, and they are shown in Figure 6. Figure 6a shows the images of a cycled NCO/CNF@Ni foam electrode, and from the image it is obvious that the electrode is completely coated with the electrolyte gel composed of KOH/Agar. The electrolyte deposits are continuous and completely mask the individual shapes of NCO flowers and CNF fibers. The contours of fiber like shapes from CNFs are observed and they are coated with electrolyte residues. One of the advantages of using the CNF interlayer, is its' ability to act as an electrolyte reservoir which is especially useful for high capacitance pseudocapacitive electrodes to avoid charge carrier depletion in the electrolyte. This image proves the same. The CNF layer was carefully peeled off, and the SEM image of the underlying NCO@Ni is displayed in Figure 6b. The NCO micro-flowers are distinctly observed, indicating that the CNF interlayer also helps in preserving the structural integrity of the NCO flowers. In striking contrast is the image of the cycled NCO@Ni foam electrode (Figure 6c). Since this electrode does not have the CNF layer, there are hardly any electrolyte deposits visible, and a higher magnification image of the same electrode (Figure 6d) shows the NCO micro-flowers to be slightly distorted. The micrograph of the cycled NCO@PEDOP/CNF@Ni (Figure 6e) is almost similar to that of the cycled NCO/CNF@Ni; here too, the entire electrode is coated with the KOH/Agar electrolyte. Again, by removing the CNF layer, the image of the underlying NCO@PEDOP@Ni (Figure 6f) reveals co-existent NCO micro-flowers and PEDOP particles, again reiterating that CNF assists with maintaining the

electrode's integrity. The fibers of NCO in the flower like shapes continue to appear as discrete entities, implying that both PEDOP and CNF ensure that the active sites on NCO remain available even after cycling. The image of NCO@PEDOP@Ni foam without CNF (Figure 6g), does not show clear electrolyte deposits, and the high magnification image in Figure 6h shows some NCO flowers, and particulate shapes. Compared to NCO@Ni, here, in the presence of PEDOP, the flowers are less distorted. Further, the cycled CNF interlayer from the NCO@PEDOP/CNF based symmetric cell, was extracted carefully, washed with deionized water, dried, and its' SEM image (Figure 6i) shows a uniform crisscross network of carbon fibers, and no fracturing or rupturing of the carbon fibers is observed. This suggests that the CNFs are unaffected by the repetitive to- and fro- movement of ions through them in the supercapacitors, and are therefore ideal for use as interlayers.

Practical utility of symmetric cell with CNF interlayers

Since the NCO@PEDOP/CNF//CNF/NCO@PEDOP symmetric cell delivered the best performance among all the cells studied in this work, the cell was subjected to some practical experiments. The cell was bent was shown in Figure 5b. From the CV plot for the bent cell (Figure 5c), it is inferred that the shape of the CV curve is an ideal-rectangular one (similar to that of a flat cell). The analogous charge-discharge plot (Figure 5d) is reasonably triangular, and a measured cell SC of 1,700 F g^{-1} indicates only a loss of 0.8% when compared to the equivalent flat cell. These experiments ratify the flexibility offered by the cell without any major performance loss. To further asses the usefulness of this cell, 3 such cells were connected in series and their photograph is shown in Figure 5e. The CV plots for 1-cell, 2-cells and 3-cells are compared in Figure 6f. At a fixed scan rate of 100 mVs^{-1}, these cell configurations were charged and discharged over 3 different voltage ranges of 0 to 1 V, 0 to 4 V and 0 to 6 V respectively. The CV plots for the 2-cells and 3-cells (connected in series), also have nearly-rectangular shapes, indicating that multiple cells connected in series retain the theoretically expected outcome profiles. The galvanostatic charge-discharge plots for 1-cell, 2-cells and 3-cells are compared in Figure 5g at 2 different current densities of 18 and 45 A g^{-1}. At a low current density of 18 A g^{-1}, they were charged to 1.5, 2.25 and 4.52 V, but at 45 A g^{-1}, they could be charged to 1.67, 2.5, and 5.1 V respectively. The discharge times however were very short at 45 A g^{-1}. The discharge capacitances were calculated using equation (5), and at 45 A g^{-1}, they are at 45 A g^{-1}, they are 538, 306 and 157 F g^{-1} and at 18 A g^{-1}, SCs are: 852, 424 and 151 F g^{-1} for 1-cell, 2-cells and 3-cells connected in series respectively. The value for 3-cells is lower than 1-cell and 2-cells based configurations, because, when the cells are connected in series, the net voltage is the algebraic sum of the voltages of the individual cells (3×1.66 V = 4.99 ≈ 5 V) and the capacitance, theoretically should be one-third of the individual cell capacitance. This is in line with the observed data. The 3-cells (connected in series) were charged to ~4 V, and then connected to a green LED (Figure 5h), which illuminated, and the bright luminance of the LED is clearly visible when the room was darkened (inset of Figure 5h). This demonstration shows the value of the NCO@PEDOP/CNF//CNF/NCO@PEDOP symmetric cell.

Role of CNF interlayer

The free standing CNF film is highly effective as a charge confining interlayer when it is used in the NCO//NCO and NCO@PEDOP//NCO@PEDOP cells. The CNF interlayer traps and allows the passage of cations (K^+, under negative bias) or anions (OH^-, under positive bias) from the electrolyte due to its porosity and ion-conducting nature, to reach the NCO or NCO@PEDOP. In high capacitance pseudocapacitive electrodes it is important to ensure that there are sufficient charge carriers available since these get depleted on charge of the device. Thus, the high porosity of the CNF enhance the performance of the supercapacitors further increasing the amount of charge carriers available. Also, when the electrons that are injected from Ni foam to the NCO based active material, they are able to reach the top layers of the material due to the electron conducting nature of CNF. Thus, the CNF also functions as an upper current collector. The SEM images of the CNF film are shown in Figure 7a and b. The CNF film is composed of an interlinked network of distinctive carbon fibers having a narrow distribution in their widths (281-400 nm). The individual fibers which form this mat-like self-supporting CNF film have smooth surfaces and they are randomly oriented, resulting in a highly porous macro-structure, conducive for easy penetration of the electrolyte. A photograph of the CNF film is shown in Figure 7c. To confirm that the CNF interlayer is capable of transporting K^+ and OH^- ions to the NCO or NCO@PEDOP materials, the ion-diffusion coefficient (D) was estimated from cyclic voltammetric studies. A symmetric cell was constructed in a CNF//CNF configuration, with the 3 M K^+-gel coated separator sandwiched between the two CNF films (Figure 7d). CV plots were recorded at different scan rates (Figure 7e). Featureless voltammograms were observed. Although no distinct cathodic or anodic peaks are observed, however, the maximum limiting cathodic and anodic current densities extracted from the plateaus in the CV curves, referred to as $i_{l,c}$ and $i_{l,a}$, were plotted as a function of the square root of scan rate ($\nu^{1/2}$). This plot is displayed in Figure 7f. The dependences are almost linear for the cathodic and anodic current densities, and therefore by using the Randles-Sevcik equation (provided below), D_{K^+} and D_{OH^-} are calculated.

$$i_{l,c} \text{ or } i_{l,a} \text{ (A cm}^{-2}) = 268600 \times n^{3/2} \times D^{1/2} \times C^* \times \nu^{1/2} \quad (6)$$

In (6), C^* is the bulk concentration of the electrolyte in mol cm^{-3}, and n is 1, which is the number of electrons involved. The anodic current density plateau corresponds to anion or OH^- diffusion, for when the CNF electrode potential is swept in the anodic direction, anions will migrate towards the electrode. In a similar vein, the cathodic plateau represents K^+ diffusion across the CNF electrode. The slopes of the $i_{l,c}$ and $i_{l,a}$ versus $\nu^{1/2}$, therefore yield the D_{K^+} and D_{OH^-} values respectively. D_{K^+} and D_{OH^-} values are almost equal, they are: 1.1×10^{-10} and 1.26×10^{-10} cm^2 s^{-1} respectively. These values show that the CNF films are capable of conducting both cations and anions, and therefore, during the supercapacitor operation, these interlayers transport the K^+ and OH^- ions to the negatively and positively biased NCO or NCO@PEDOP electrodes.

To show that the CNF electrodes by themselves, do not show any significant SC, galvanostatic charge-discharge plots were recorded for the CNF//CNF cell at different current densities. The plots (Figure 7g) have triangular profiles, but the SCs are very low. They vary from 13.6 to 2.7 F g^{-1} when current density is varied from 0.5 to 1.25 mA cm^{-2}. Compared to the performance of the NCO based cell without the CNF interlayer, this SC is almost insignificant, thus showing that CNF boosts the

overall charge storage performance of redox active materials by allowing facile ion, electron movement and providing an additional charge carrier reservoir.

Conclusions

The synergy between NCO and PEDOP: i.e. the ability of NCO to deliver high SCs, and the capability of PEDOP to function as a conducting matrix for facile charge movement and to undergo redox reactions, comes to the fore to yield a high performance binder free electrode of NCO@PEDOP supported over Ni foam. By incorporation of free standing CNF interlayers in the NCO@PEDOP based symmetric supercapacitor at both half-cells, which allowed unobstructed propagation of K^+ and OH^- ions to (or from) the NCO or NCO@PEDOP electrodes, a greatly enhanced SC of 1,775 Fg^{-1} (at 0.96 A g^{-1}), an energy density of 986 Wh kg^{-1} (at a power density of 0.961 kW kg^{-1}), a very stable cycling response, coupled with a slow self-discharge rate and low ion-diffusion resistance, contrasting significantly with the sole NCO based supercapacitor is achieved for the NCO@PEDOP/CNF based symmetric supercapacitor. SEM studies of the cycled electrodes reveal that CNF interlayers serve as electrolyte reservoirs, improve durability and increase SC. The aspect of being an electrolyte reservoir is particularly important in high capacitance electrodes to avoid depletion of the charge carriers. The ease of fabrication of this bi-layered supercapacitor combined with high SC, rate responsive, wide voltage window of operation, cyclability, and demonstrations of invariant performance with bending and LED illumination, showcase the scalability of this assembly for real-time applications.

Supporting information

Cyclic voltammograms of PEDOP//PEDOP cell recorded at different scan rates over a voltage range of 0 to 1 V. Comparison table for performance characteristics of NCO based supercapacitors. Cyclic voltammograms and charge-discharge plots of NCO@PEDOP//NCO@PEDOP cell.

Conflicts of interest

There are no conflicts to declare.

Acknowledgements

Financial support from the Department of Science & Technology of India (Project: India-UK Center for education and research in clean energy (IUCERCE), Grant no. DST/RCUK/JVCCE/2015/04 (1) (G)) is gratefully acknowledged by M. Deepa and S. Deshagani. S.D. is thankful to University Grants Commission (UGC) for the grant of junior research fellowship. This work was also financially supported by the EPSRC Joint UK-India Clean Energy Centre (JUICE) (EP/P003605/1) and Energy Storage for Low Carbon Grids (EP/K002252/1) project for Dr. Xinhua Liu and Dr. Billy Wu.

References

1 T. Yu, Z. Li, S. Chen, Y. Ding, W. Chen, X. Liu, Y. Huang and F. Kong, *ACS Sustain. Chem. Eng.*, 2018, **6**, 7355-7361.
2 F. Hu, J. Wang, S. Hu, L. Li, W. Shao, J. Qiu, Z. Lei, W. Deng and X. Jian, *ACS Appl. Mater. Interfaces.*, 2017, **9**, 31940-31949.
3 F. Hu, J. Wang, S. Hu, L. Li, G. Wang, J. Qiu, and X. Jian, *Nanoscale*, 2016, **8**, 16323-16331.
4 Y. Zhang, L. Li, H. Su, W. Huang and X. Dong, *J. Mater. Chem. A*, 2015, **3**, 43-59.
5 J. Chang, M. Jin, F.Yao, T. H. Kim, V. T. Le, H. Yue, F. Gunes, B. Li, A. Ghosh and S. Xie, *Adv. Funct. Mater.*, 2013, **23**, 5074-5083.
6 Q. Wang, Y. Zou, C. Xiang, H. Chu, H. Zhang, F. Xu, L. Sun and C. Tang, *Ceram. Int.*, 2016, **42**, 12129-12135.
7 G.A. Snook, P. Kao and A.S. Best, *J. Power Sources*, 2011, **196**, 1-12.
8 X. C. Dong, H. Xu, X. W. Wang, Y. X. Huang, M. B. Chan-Park, H. Zhang, L. H. Wang, W. Huang and P. Chen, *ACS Nano*, 2012, **6**, 3206-3213.
9 J. Xu, Z. Tan, W. Zeng, G. Chen, S. Wu, Y. Zhao, K. Ni, Z. Tao, M. Ikram, H. Ji and Y. Zhu, *Adv. Mater.*, 2016, **28**, 5222-5228.
10 J. Zhang, X. Zhang, Y. Zhou, S. Guo, K. Wang, Z. Liang and Q. Xu, *ACS Sustain. Chem. Eng.*, 2014, **2**, 1525-1533.
11 H. Xia, Y. S. Meng, G. Yuan, C. Cui and L. Lu, *Electrochem. Solid-State Lett.*, 2012, **15**, A60.
12 F. Liu, X. Wang, J. Hao, S. Han, J. Lian and Q. Jiang, *Sci. Rep.*, 2017, **7**, 1-10.
13 G. Yu, L. Hu, N. Liu, H. Wang, M. Vosgueritchian, Y. Yang, Y. Cui and Z. Bao, *Nano Lett.*, 2011, **11**, 4438-4442.
14 G. Zhang, X. W. D. Lou, *Sci. Rep.*, 2013, **3**, 2-7.
15 B. Cui, H. Lin, J. B. Li, X. Li, J. Yang and J. Tao, *Adv. Funct. Mater.*, 2008, **18**, 1441-1447.
16 T. Y. Wei, C. H. Chen, H. C. Chien, S. Y. Lu and C. C. Hu, *Adv. Mater.*, 2010, **22**, 347-351.
17 H. S. Jadhav, R. S. Kalubarme, C. N. Park, J. Kim and C. J. Park, *Nanoscale*, 2014, **6**, 10071-10076.
18 C. L. Gaupp, K. Zong, P. Schottland, B. C. Thompson, C. A. Thomas and J. R. Reynolds, *Macromolecules*, 2000, **33**, 1132-1133
19 S. Deshagani, K. Krushnamurty, and M. Deepa, *Mater. Today Energy*, 2018, **9**, 137-153.
20 H. Wang, J. Lu, S. Yao and W. Zhang, J. Alloys Compd, 2018, 744, 187-195.
21 X. Hu, Y. Masuda, T. Ohji and K. Kato, *Cryst. Growth Des.*, 2010, **10**, 626-631.
22 X. Liu, M. N. Marlow, S. J. Cooper, B. Song, X. Chen, N. P. Brandon, and B. Wu, *J. Power Sources*, 2018, **384**, 264-269.
23 B. N. Reddy, S. Deshagani, M. Deepa and P. Ghosal, *Chem. Eng. J.*, 2018, **334**, 1328-1340.
24 W. Xiong, Y. Gao, X. Wu, X. Hu, D. Lan, Y. Chen, X. Pu, Y. Zeng, J. Su and Z. Zhu, *ACS Appl. Mater. Interfaces*, 2014, **6**, 19416-19423.
25 N. Garg, M. Basu and A.K. Ganguli, *J. Phys. Chem. C*, 2014, **118**, 17332-17341.
26 H. Lai, L. Shang, Q. Wu, L. Yang, J. Zhao, H. Li, Z. Lyu, X. Wang and Z. Hu, *ACS Appl. Energy Mater.*, 2018, **1**, 684-691.
27 L. Chen, L. Mu, T. Ji and J. Zhu, *J. Phys. Chem. C*, 2016, **120**, 23377-23388.
28 D. Kong, W. Ren, C. Cheng, Y. Wang, Z. Huang and H. Y. Yang, *ACS Appl. Mater. Interfaces*, 2015, **7**, 21334-21346.
29 V. Veeramani, R. Madhu, S. M. Chen and M. Sivakumar, *ACS Sustain. Chem. Eng.*, 2016, **4**, 5013-5020.
30 J. Xu, F. Liu, X. Peng, J. Li, Y. Yang, D. Jin, H. Jin, X. Wang and B. Hong, *ChemSelec*t, 2017, **2**, 5189-5195.
31 G. He, L. Wang, H. Chen, X. Sun and X. Wang, *Mater. Lett.*, 2013, **98**, 164-167.
32 X. Lia, *RSC Adv.*, 2015, **11**, 7976-7985.

Table 1: Electrochemical properties of symmetric supercapacitors

View Article Online
DOI: 10.1039/C8NR08645A

Parameter	NCO	NCO/CNF	NCO@PEDOP	NCO@PEDOP/CNF
SC (F g^{-1}) ΔV: 2 V	1,453 (1.25 A g^{-1})	1,554 (0.96 A g^{-1})	1,617 (1.25 A g^{-1})	1,775 (0.96 A g^{-1})
Energy density (Wh kg^{-1}) (2 V)	807	863	898	986
Power Density (kW kg^{-1}) (2 V)	1.25	0.96	1.25	0.96
Self-discharge from 2 V in 80 min. (V)	0.01	0.018	-	0.05
% of retained capacitance After 5000 cycles V: 2 V, 20 A g^{-1}	96	98	99	99

View Article Online
DOI: 10.1039/C8NR08645A

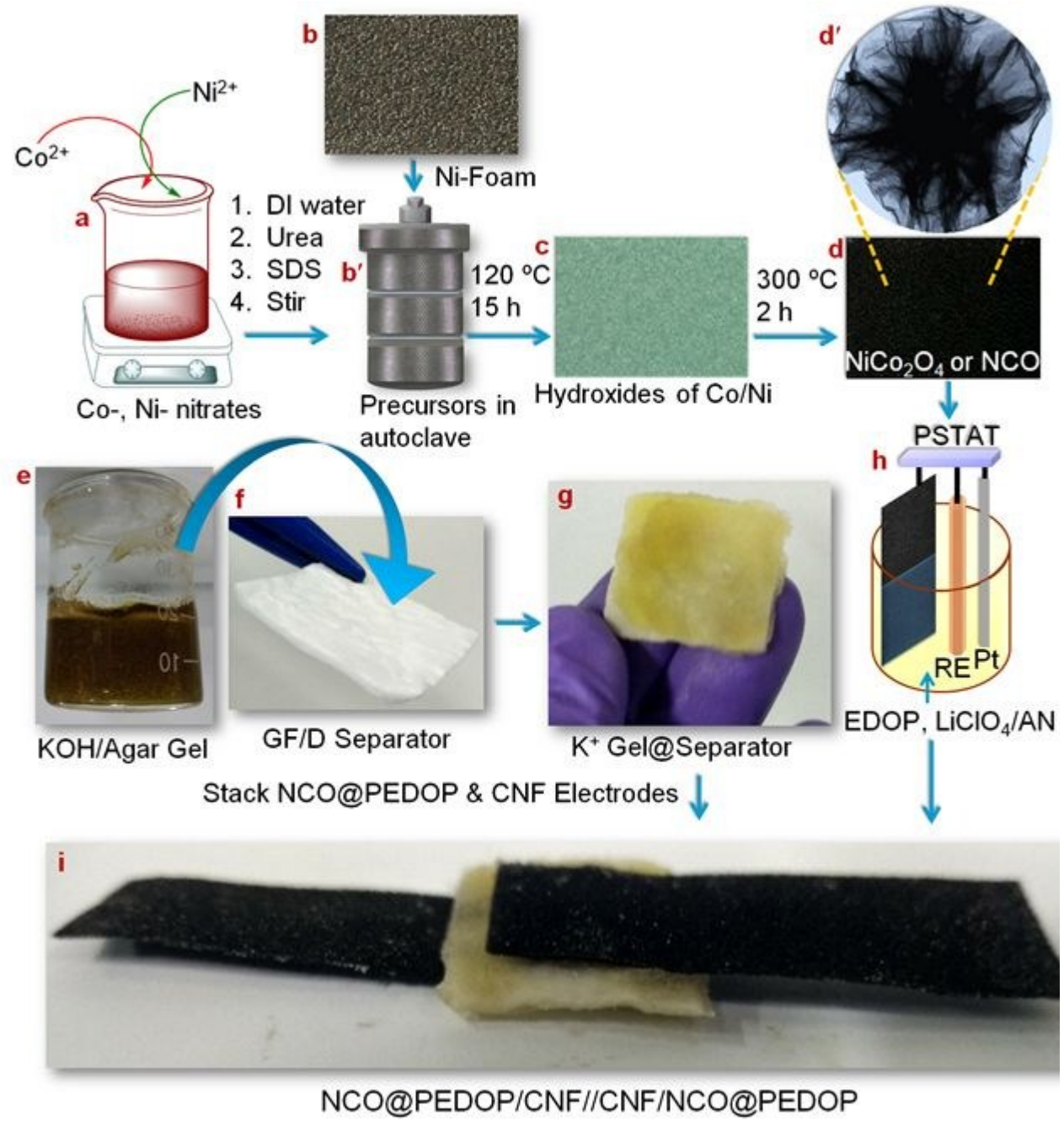

Scheme 1 (a) Mixture of precursors for NCO, (b) Ni foam substrate, (b') autoclave containing the precursor solution and the Ni foam, (c) Ni foam coated with NCO intermediates, (d) NCO@Ni foam and (d') is the TEM image of NCO. Photographs of (e) KOH/Agar gel, (f) GF/D separator and (g) Gel/separator. (h) Schematic of electropolymerization set-up for PEDOP and (i) photograph of the symmetric NCO@PEDOP/CNF cell.

Figures

View Article Online
DOI: 10.1039/C8NR08645A

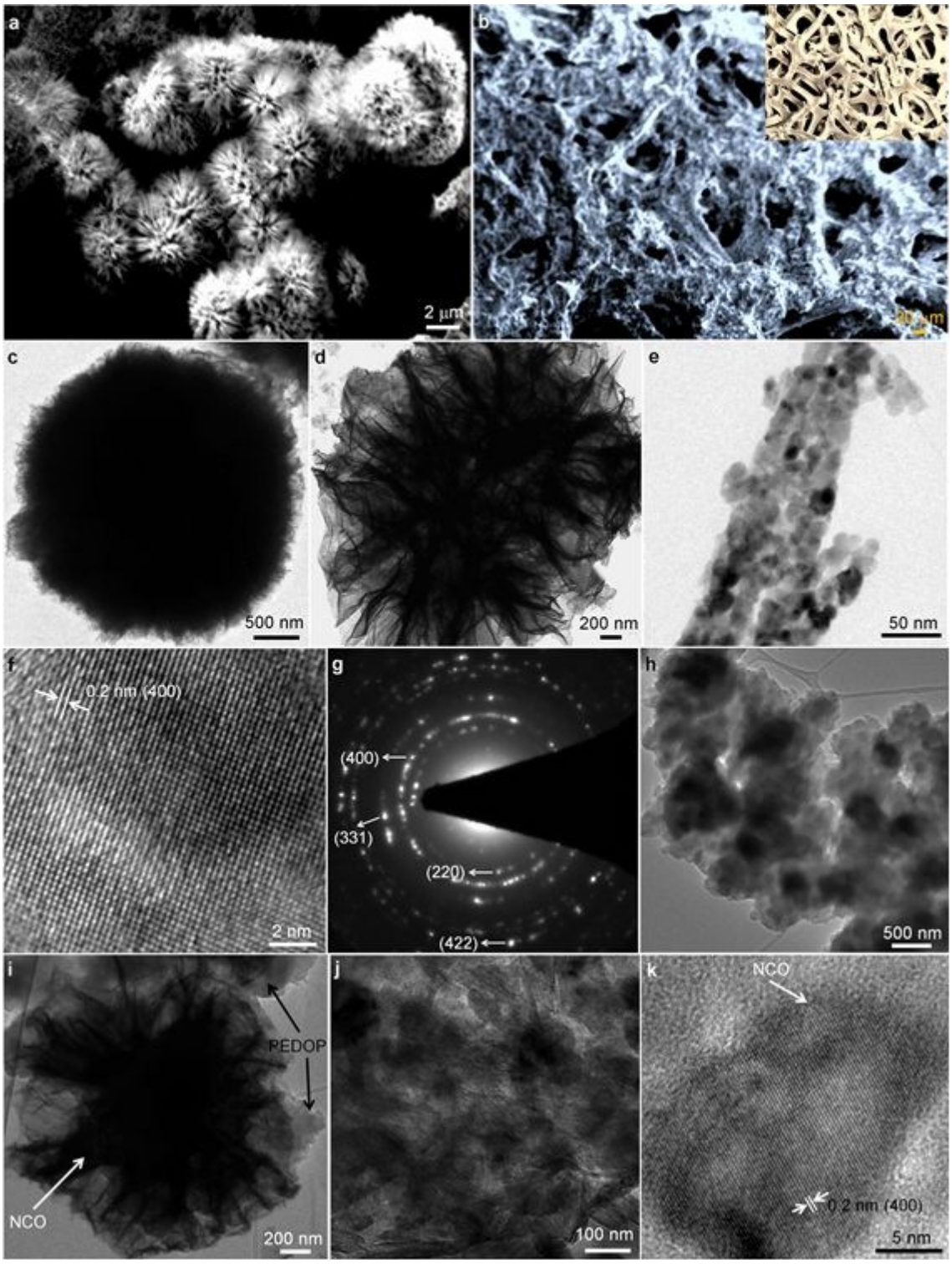

Figure 1 SEM images of (a) NCO, (b) NCO@PEDOP deposited over Ni foam (inset of (b) shows uncoated Ni foam substrate). (c,d,e) TEM images, (f) lattice scale image and (g) SAED pattern of NCO micro-flowers. (h) TEM image of PEDOP. (i,j) TEM images and (k) lattice scale image of NCO@PEDOP.

View Article Online
DOI: 10.1039/C8NR08645A

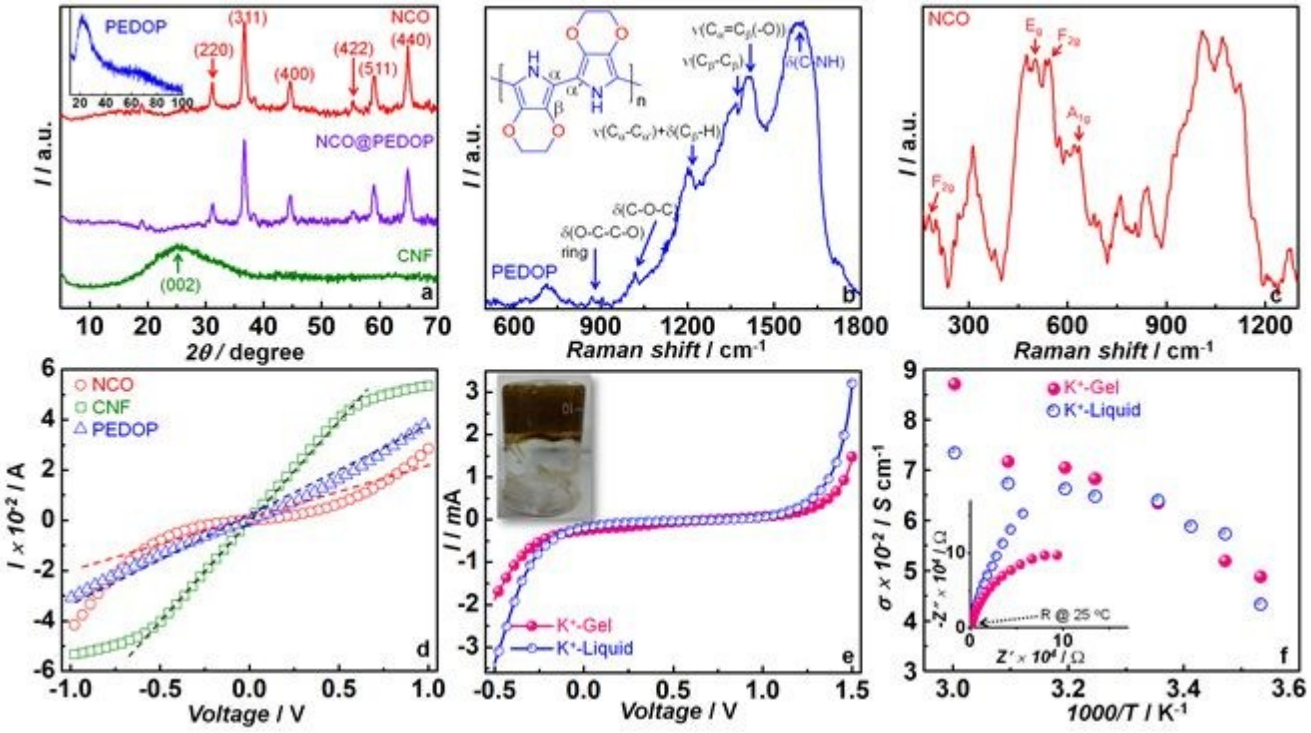

Figure 2 (a) XRD patterns of NCO micro-flowers, NCO@PEDOP and CNF; inset is a diffractogram of pristine PEDOP. Raman spectra of (b) PEDOP and (c) NCO micro-flowers. I-V characteristics of (d) of NCO micro-flowers, PEDOP and CNF recorded in SS/active material/SS configurations, the dashed lines represent the linear fits. (e) Linear sweep voltammograms and (f) thermal dependence of ionic conductivity of K^+ ion conducting gel and liquid electrolytes with 3 M KOH, with Z″ versus Z′ plot for the same at 25 °C as inset. Insets of (c) and (e) are structure of PEDOP and photograph of the gel respectively.

View Article Online
DOI: 10.1039/C8NR08645A

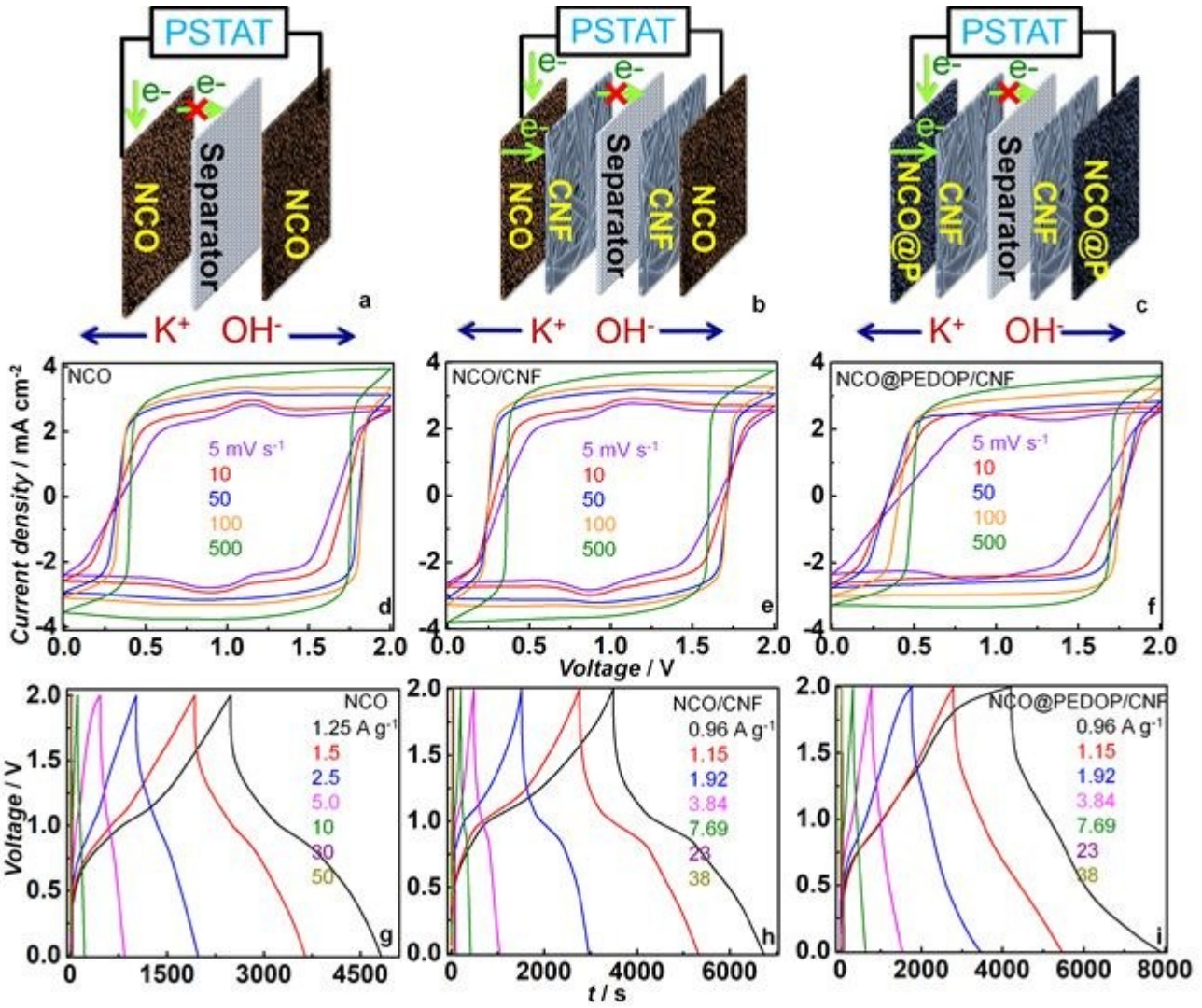

Figure 3 (a-c) Schematics of symmetric cells with different electrode configurations and the corresponding cyclic voltammograms of (d) NCO, (e) NCO/CNF and (f) NCO@PEDOP/CNF cells recorded at different scan rates over a voltage range of 0 to 2 V. Galvanostatic charge-discharge characteristics of (g) NCO, (h) NCO/CNF and (i) NCO@PEDOP/CNF cells recorded at different current densities over a voltage range of 0 to 2 V.

View Article Online
DOI: 10.1039/C8NR08645A

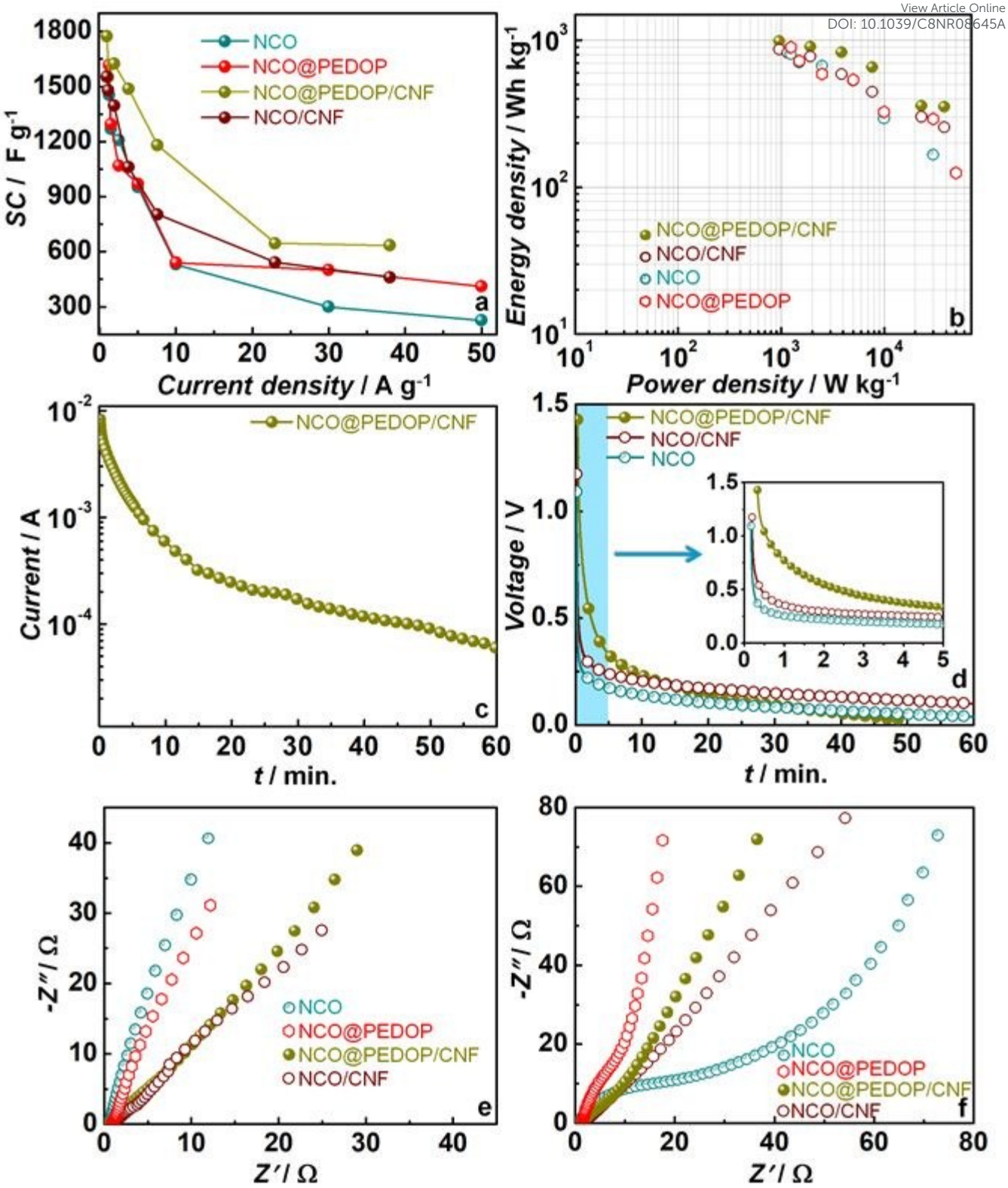

Figure 4 (a) Rate capability profiles (SC versus current density) and (b) Ragone plots of symmetric cells with electrodes of NCO, NCO/CNF, NCO@PEDOP and NCO@PEDOP/CNF with the K^+ ion conducting gel electrolyte. (c) Leakage current versus time curves of NCO@PEDOP/CNF when fully charged to 1.5 V and (d) self-discharge plots. Nyquist plots of symmetric cells, (e) before cycling and (f) after 5000 cycles recorded over a frequency range of 1 MHz to 0.1 Hz under an ac bias of 10 mV. Inset of (d) is a magnified view of the voltage decay in the initial 5 min.

View Article Online
DOI: 10.1039/C8NR08645A

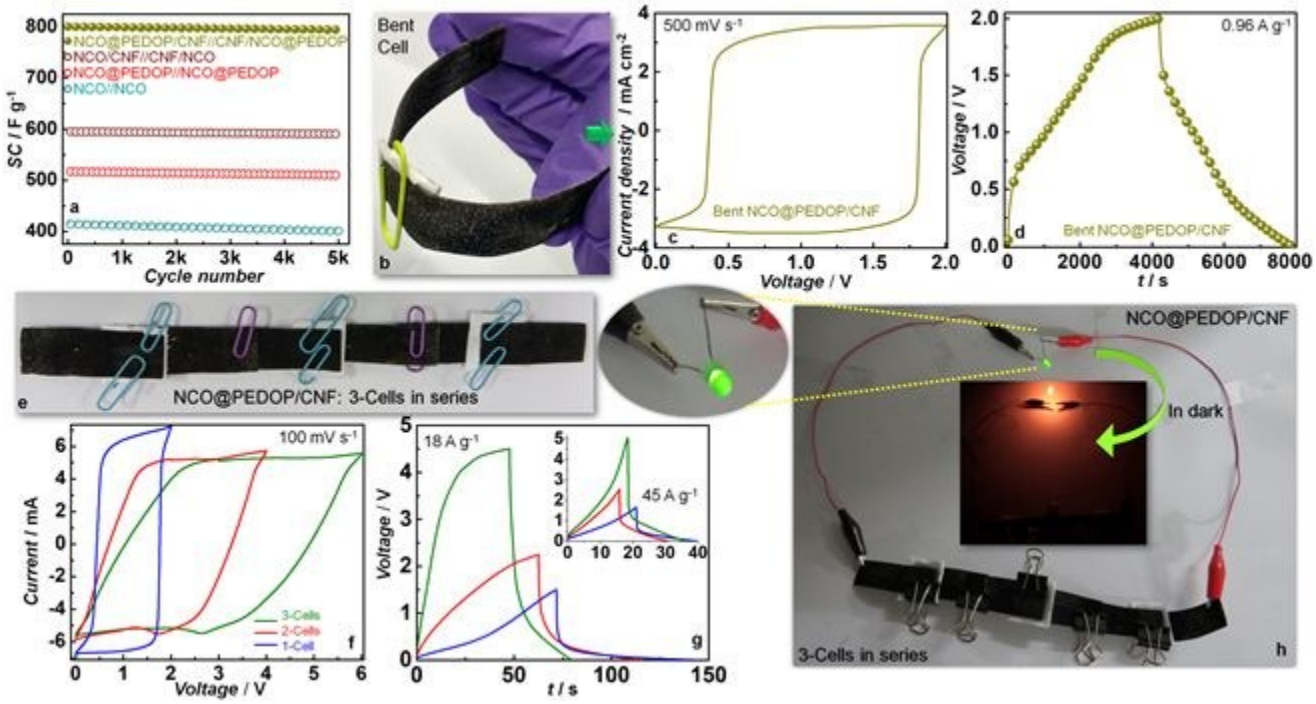

Figure 5 (a) Variation in SC as a function of cycling at 20 A g^{-1} for symmetric cells with electrodes of NCO, NCO/CNF, NCO@PEDOP and NCO@PEDOP/CNF with the K^+ ion conducting gel electrolyte. (b) Photograph of a bent symmetric cell with 2 NCO@PEDOP/CNF electrodes and its' (c) CV plot and (d) charge-discharge characteristics. (e) Photograph of 3 planar symmetric cells with NCO@PEDOP/CNF electrodes connected in series. (f) CV plots (at 100 mV s^{-1}), (g) and inset show galvanostatic charge-discharge curves (at 18 and 45 A g^{-1}) of 1, 2 and 3 symmetric cells with NCO@PEDOP/CNF electrodes. (h) Illumination of a green LED using 3 fully charged planar symmetric cells with NCO@PEDOP/CNF electrodes connected in series in daylight and in dark (inset).

View Article Online
DOI: 10.1039/C8NR08645A

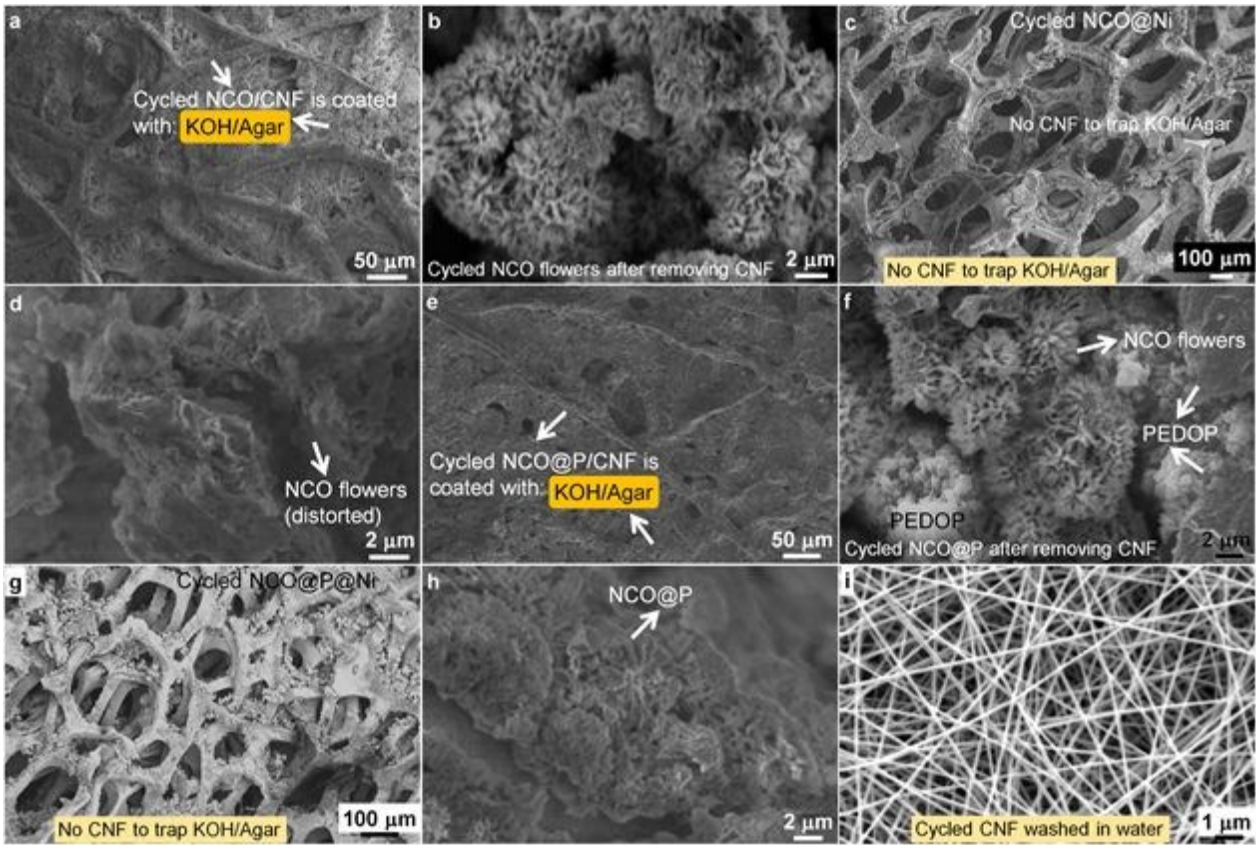

Figure 6 SEM images of: (a) cycled NCO/CNF and (b) the same electrode after removing the CNF layer, (c,d) cycled NCO electrodes without CNF, (e) cycled NCO@PEDOP/CNF and (f) the same electrode after removing the CNF layer, (g,h) cycled NCO@PEDOP electrodes without CNF and (i) cycled CNF interlayer extracted from a cycled symmetric NCO@PEDOP/CNF cell. All electrodes were cycled 5000 times. PEDOP is abbreviated as P in (e-h).

View Article Online
DOI: 10.1039/C8NR08645A

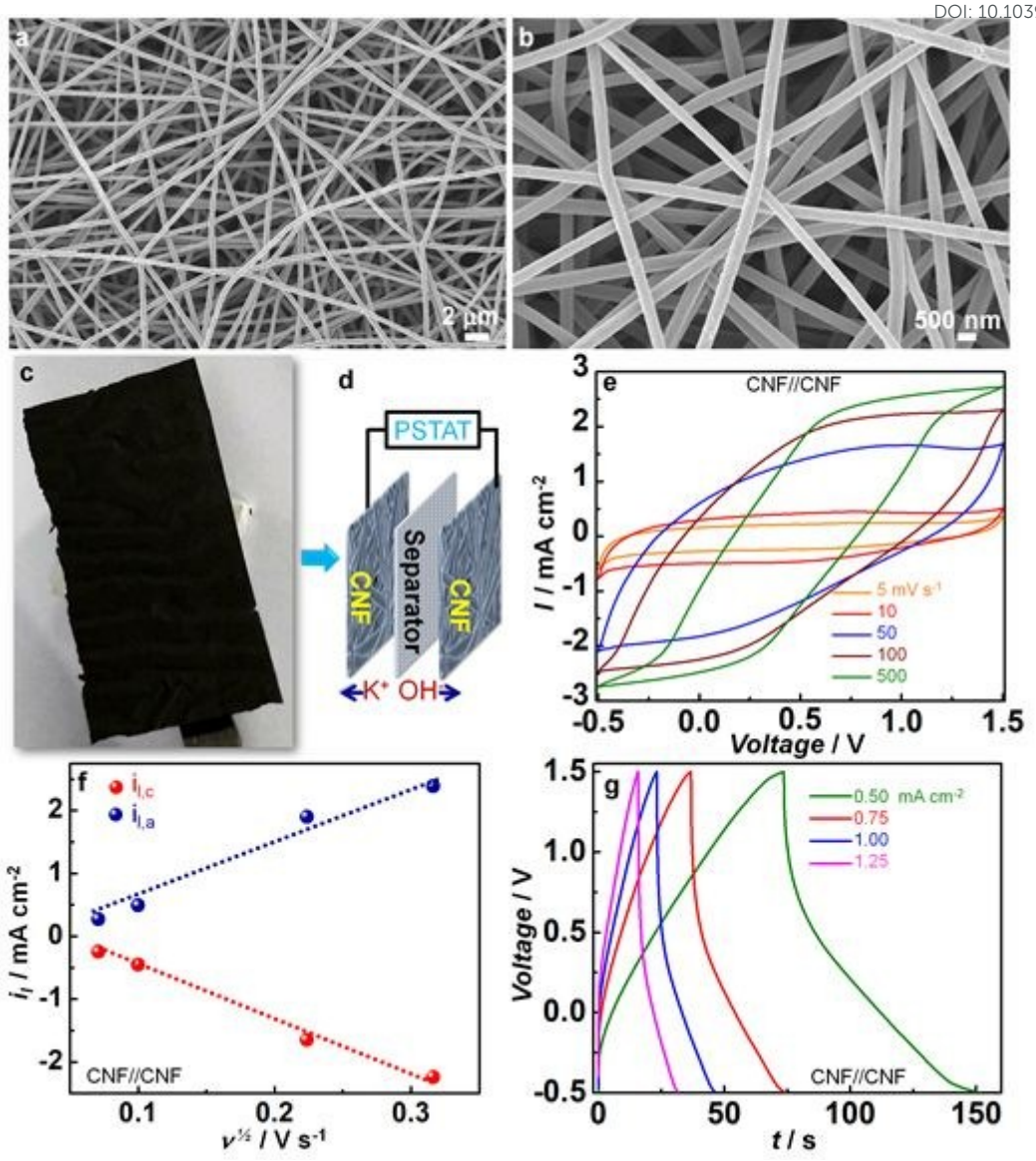

Figure 7 (a, b) SEM images and (c) photograph of a CNF free standing film. (d) Schematic of a symmetric cell with 2 CNF films as electrodes. (e) CV plots of the CNF based cell recorded at different scan rates. (f) Peak current density versus square root of scan rate plots for the CNF based cell. (g) Galvanostatic charge-discharge plots of the CNF based cell recorded at different current densities.

View Article Online
DOI: 10.1039/C8NR08645A

Graphical Abstract